

RESEARCH ARTICLE

Open Access



Electrochemical study of TiO₂ in aqueous AlCl₃ electrolyte via vacuum impregnation for superior high-rate electrode performance

A. W. Holland, A. Cruden, A. Zerey, A. Hector and R. G. A. Wills* 

Abstract

This communication elucidates the charge storage mechanism of a TiO₂ electrode in 1 mol dm⁻³ AlCl₃ for use in aqueous-ion batteries. Cyclic voltammetry studies suggest a surface contribution to charge storage and that cycle life can be improved by limiting the potential ≥ -1.0 V vs SCE. In order to enhance this surface contribution, a simple vacuum impregnation technique was employed to improve electrode-electrolyte contact. This resulted in a significant improvement in the high rate performance of TiO₂, where a capacity of 15 mA h g⁻¹ was maintained at the very high specific current of 40 A g⁻¹, a decrease of only 25% from when the electrode was cycled at 1 A g⁻¹. The vacuum impregnation process was also applied to copper-hexacyanoferrate, envisaged as a possible positive electrode, again resulting in significant improvements to high-rate performance. This demonstrates the potential for using this simple technique for improving electrode performance in other aqueous electrolyte battery systems.

Keywords: Aqueous aluminium ion battery

Introduction

Asymmetric and hybrid devices based on a combination of capacitive, pseudocapacitive or battery intercalation electrodes have gained interest lately due to performance characteristics that could bridge the gap between the high energy density of Li-ion chemistries and high power of supercapacitors. Furthermore, there is interest in the use of aqueous electrolytes, which can provide advantages in terms of cost, ease of handling, toxicity, and environmental benignity. The use of electrolytes based on Na, K or Al salts also benefit from the higher natural abundance and relative ease of processing of these materials compared to Li salts and organic solvents.

Excluding Li-ion, negative electrodes for aqueous metal-ion systems are relatively limited with NaTi₂(PO₄)₃ and metallic Zn commonly used in aqueous Na-ion and Zn-ion cells [1–4]. Similarly, while a variety of positive electrodes have been explored for aqueous super/pseudocapacitors, such as MnO₂ [5–7], RuO₂ [8–10], Ni(OH)₂

[11], Co(OH)₂ [12], Co₃O₄ [13] or Prussian blue analogues [14, 15], the number of negative electrodes is far lower. As such, a non-exhaustive review of aqueous super/pseudo-capacitive devices, reported since 2014, shows that the majority of negative electrodes consist of activated carbon (AC) or other carbon-based materials, as shown in Additional file 1: Table S1. A recent review on asymmetric supercapacitors by Shao et al., further illustrates this, where the majority of studies and devices make use of AC, graphene or graphene oxide as the negative electrode [16]. The use of AC is likely to limit cell voltage and capacity while graphene materials can result in high cost and low scalability. TiO₂ provides a possible option for a negative electrode, having been studied in aqueous aluminium salt electrolytes and shown to have working potentials lower than ca. < -0.5 V vs SCE [15–20], presenting the opportunity for dual-ion devices working at higher voltages [21–24]. TiO₂ nanotube arrays, synthesised by Liu et al., allowed a capacity of ca. 75 mA h g⁻¹ when cycled at 4 mA cm⁻² in 1 mol dm⁻³ AlCl₃ [17]. He et al., have provided evidence for Al³⁺ intercalation, where XRD analysis showed anatase-TiO₂ lattice parameters changing with

* Correspondence: rgaw@soton.ac.uk
Faculty of Engineering and Physical Sciences, University of Southampton,
Highfield, Southampton SO17 1BJ, UK



state-of-charge [19]. However, capacitive or surface contributions to charge storage cannot be entirely ruled out, especially at high rates. For example, cathodic redox peaks from TiO_2 , associated with Al^{3+} insertion, are at more negative potentials than the plateaus observed during constant current cycling [17, 19, 20]. Furthermore, a graphene incorporated TiO_2 electrode studied by Lahan et al., provided a capacity of approximately 20 mA h g^{-1} at 6.25 A g^{-1} , though the electrode showed very limited redox peaks during CV scans, suggesting the possibility of a capacitive or pseudocapacitive mechanism [1]. Previous work has also shown high rate capability, up to 360 C (7.2 A g^{-1}), from commercial TiO_2 nanopowders, though relatively low capacities were measured [25].

Building upon previous work, this communication elucidates the charge storage mechanism of commercial TiO_2 powder electrodes in $1 \text{ mol dm}^{-3} \text{ AlCl}_3$ and demonstrates a TiO_2 electrode capable of stable cycling at 40.0 A g^{-1} with close to 100% charge efficiency.

Experimental procedures

TiO_2 electrodes were manufactured using a 5 nm TiO_2 powder purchased from US-nano. Electrodes consisted of 85 wt% TiO_2 , 5 wt% carbon black (Vulcan 72-CR), 6 wt% Nafion and 4 wt% PTFE. TiO_2 , carbon black, Nafion and propanol (approximately 3 g for 1 g dry powder) were mixed using a Silverson high speed shear mixer at 5000 rpm for 30 min. PTFE was then added with the ink sonicated for a further 15 min. The ink is coated onto carbon polymer (Sigracell PV15) current collectors with excess allowed to drip off before being laid flat to dry in ambient conditions. Once dry, additional layers were added to manufacture electrodes with mass loadings as high as 6.5 mg cm^{-2} covering an area of 7 cm^2 .

Brunauer-Emmett-Teller (BET) surface area and pore size distribution were calculated from N_2 adsorption-desorption isotherms, measured at -196°C , using a Gemini 2375 analyser.

Cyclic voltammetry and constant current cycling were performed in standard glass 3-electrode cells using a saturated calomel electrode (SCE) as reference and an oversized CuHCF , typically 7–8 times by mass, as a reversible counter electrode. Cyclic voltammetry was performed in $1 \text{ mol dm}^{-3} \text{ AlCl}_3$ while constant current cycling was performed in an electrolyte comprising $1 \text{ mol dm}^{-3} \text{ AlCl}_3$ and $1 \text{ mol dm}^{-3} \text{ KCl}$. A solartron 1470E battery analyser was used for constant current cycling while cyclic voltammetry was performed on an Ivium-n-Stat potentiostat.

Vacuum impregnation, previously used by Yong et al. for impregnation of textile supercapacitor electrodes [26], was performed using the experimental set-up shown in Fig. 1a with a proposed schematic of how electrolyte is forced into electrode pores being presented in

Fig. 1b. This method was performed by placing electrodes, submerged in the electrolyte of $1 \text{ mol dm}^{-3} \text{ AlCl}_3/1 \text{ mol dm}^{-3} \text{ KCl}$, in a Buchi tube. A filtration vacuum pump was used to create a vacuum of 20 mbar within the tube for approximately 15 min. The air vent was then opened, letting air in, before the process was repeated a further three times by which point air bubbles were no longer visible at the electrode surface.

Results and discussion

Figure 2a shows the N_2 adsorption-desorption BET isotherm from the TiO_2 nanopowder. The BET surface area was calculated to be $269 \text{ m}^2 \text{ g}^{-1}$. The profile resembles a type IV isotherm according to the IUPAC classification. Fig. 2b shows a pore size distribution between 25 \AA to 100 \AA with a dominant peak at around 55 \AA . This corresponds well with the isotherm in Fig. 2a, which demonstrates the mesoporous nature ($2 \text{ nm} - 50 \text{ nm}$) of the powder.

Cyclic voltammetry of two TiO_2 electrodes was performed at various scan rates, v , in $1 \text{ mol dm}^{-3} \text{ AlCl}_3$ aqueous solution. One electrode was scanned between 0 V to -1.3 V vs SCE and the other between the potential range of 0 V to -1.0 V vs SCE. By limiting the potential window, charge storage may be limited to a capacitive or surface controlled mechanism. Figure 3a presents the profiles measured from TiO_2 at the 5th, 18th and 25th cycles when swept between the extended potential range of 0 V to -1.3 V vs SCE. Between the 5th and 18th cycle there is small reduction in the cathodic peak, from -13.0 A g^{-1} to -11.8 A g^{-1} , while the anodic peak potential shifts from -1.03 V , during the 10th scan, to -0.97 V vs SCE during the 18th. Figure 3b shows the profile from TiO_2 during the 5th, 25th and 80th scan at 10 mV s^{-1} between 0 V to -1.0 V vs SCE. The profiles can be seen to be nearly identical irrespective of scan number, suggesting improved stability from TiO_2 when cycled at a more positive minimum potential.

Figure 4a shows the CV scans at $3, 9$ and 16 mV s^{-1} between 0 V to -1.3 V vs SCE. The profile shapes at these three scan rates closely resemble each other. During the cathodic sweep, current curves down between -0.55 V to -0.95 V where there is a brief plateau till ca. -1.1 V . The current curves down to a prominent peak between -1.15 V and -1.20 V vs SCE. At 3 mV s^{-1} , the reverse sweep gives rise to a prominent peak at -1.05 V . The position of this peak becomes more positive with increasing scan rate with peak position being approximately -0.95 V at 16 mV s^{-1} . As with the cathodic sweep, the anodic sweep gives rise to a slight shoulder and plateau – between ca. -0.9 V and -0.75 V , when current drops steadily to zero at approximately -0.5 V . Fig. 4b gives the peak currents against the square root of the scan rates. A linear fit, with an x-y intercept set to

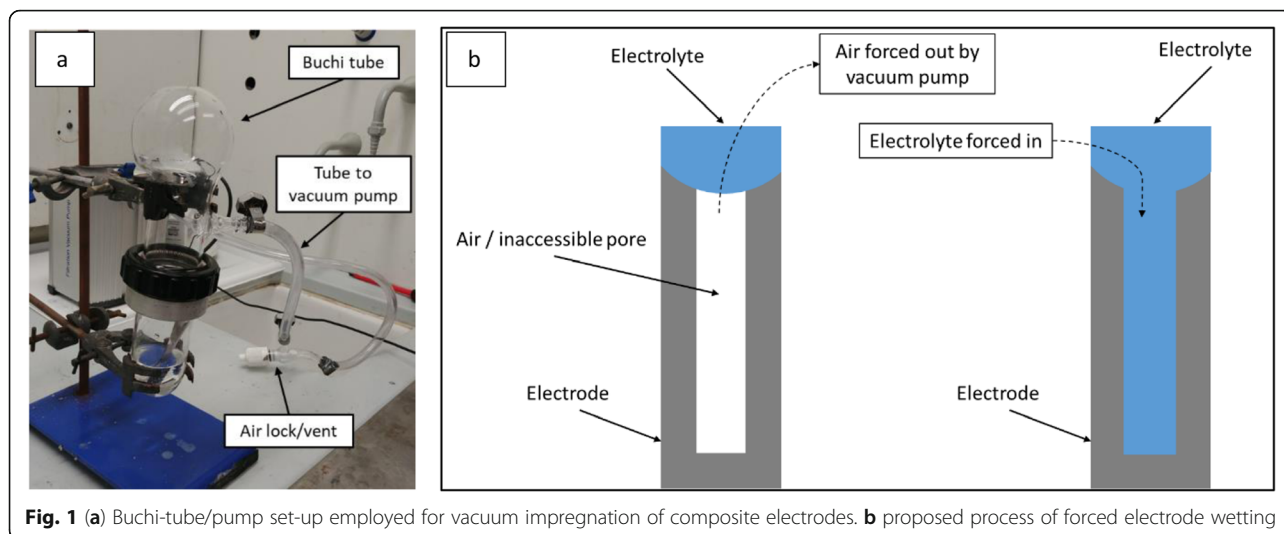


Fig. 1 (a) Buchi-tube/pump set-up employed for vacuum impregnation of composite electrodes. **b** proposed process of forced electrode wetting

zero, shows there is an approximately linear relationship between the measured current and square root of the scan rate for both cathodic and anodic sweeps. A linear relationship suggests a diffusion-limited process, as described by the power law given by equation... (1), where a and b are adjustable values, i is the measured current and ν the scan rate [27, 28].

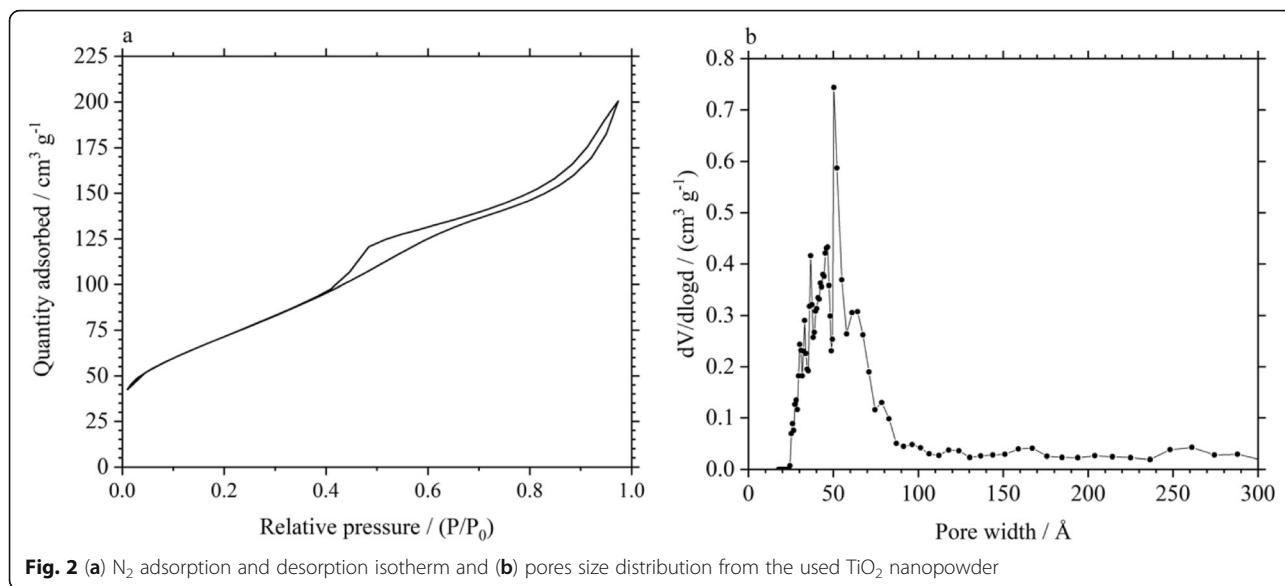
$$i = a\nu^b \quad (1)$$

A b -value of 0.5 is often measured from intercalation electrodes, with the measured current limited by the solid-state diffusion (intercalation) of the cation through the electrode. This may be true for the case of TiO_2 and Al^{3+} , given the use of a relatively high concentration electrolyte, which should negate the possibility of a reaction being limited by the diffusion of Al^{3+} through the electrolyte to the electrode surface.

However, the greater stability of TiO_2 when scanned with the more positive minimum potential of -1.0 V vs SCE, compared to -1.3 V, suggests the possibility of a separate charge storage mechanism compared to when the electrode is scanned to -1.3 V. That is, the redox reaction of Ti^{4+} to Ti^{3+} may only take place once more negative potentials are reached. As such, further CV scans were performed between 0 V to -1.0 V vs SCE. Fig. 4c shows these CV profiles at scan rates between 2 mV s^{-1} to 100 mV s^{-1} , normalised by scan rate. That the profiles do not fall onto a single profile means that charge storage in this potential range is not purely capacitive. Further analysis of the CV profiles can be performed by calculating the capacity of the electrodes at different scan rates. This technique has previously been used in the literature with materials, such as Nb_2O_5 , NiCo_2O_4 , LaB_6 , conductive polymers and for Li^+ insertion into mesoporous titania

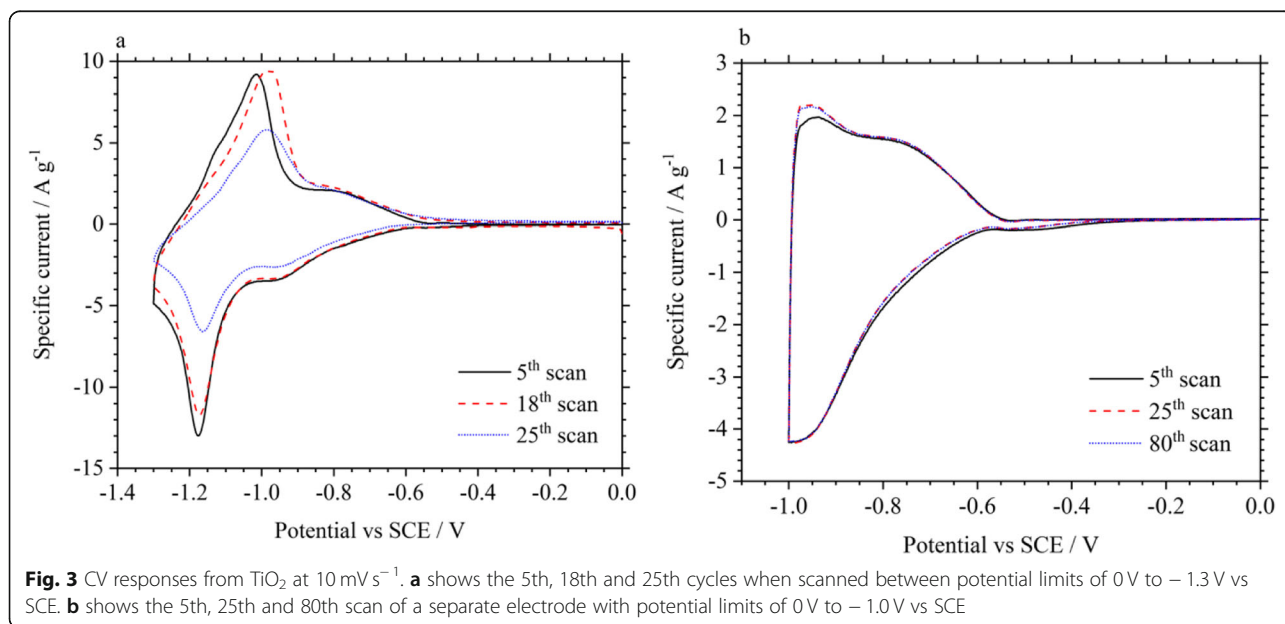
[29–32]. The analysis can provide an indication of charge storage arising from bulk or surface mechanisms at given scan rates. Fig. 4d shows the cathodic and anodic voltammetric capacities against $\nu^{-1/2}$. For the cathodic charge input, the volumetric capacity is linearly proportional to $\nu^{-1/2}$ at scan rates up to 30 mV s^{-1} , $(0.182$ $\text{mV s}^{-1})^{-1/2}$. Extrapolation of the linear fit to 0 $(\text{mV s}^{-1})^{-1/2}$ suggests a surface charge storage contribution of approximately 12 mA h g^{-1} . Therefore, at a scan rate of 10 mV s^{-1} , for example, the surface contribution to capacity would be approximately 50%. The remaining charge could then be the result of a bulk process such as intercalation. Alternatively, it could suggest there are areas of the electrode, such as narrow pores, that are difficult to access. At scan rates above 30 mV s^{-1} , the charge vs $\nu^{-1/2}$ plot deviates from linearity, suggesting a change in the rate-limiting charge storage process or that charge storage is almost entirely dominated by a semi-infinite diffusion. At lower scan rates, between 2 to 30 mV s^{-1} , the extrapolation of the linear dependence of cathodic capacity vs $\nu^{-1/2}$, to approximately 12 mA h g^{-1} , suggests that charge storage is diffusion controlled. Given the low capacities, it is still unlikely that this diffusion limitation is a result of Al^{3+} intercalation through the crystal structure of anatase- TiO_2 but may instead be due to the limited diffusion of electrolyte and Al^{3+} , due to the short time constants at these high scan rates, through the electrodes pores. While there may be a capacitive contribution, as deduced from the extrapolation of the infinite scan rate capacity, the non-conformity of the normalised scan rates suggests there is also a diffusion controlled charge storage mechanism.

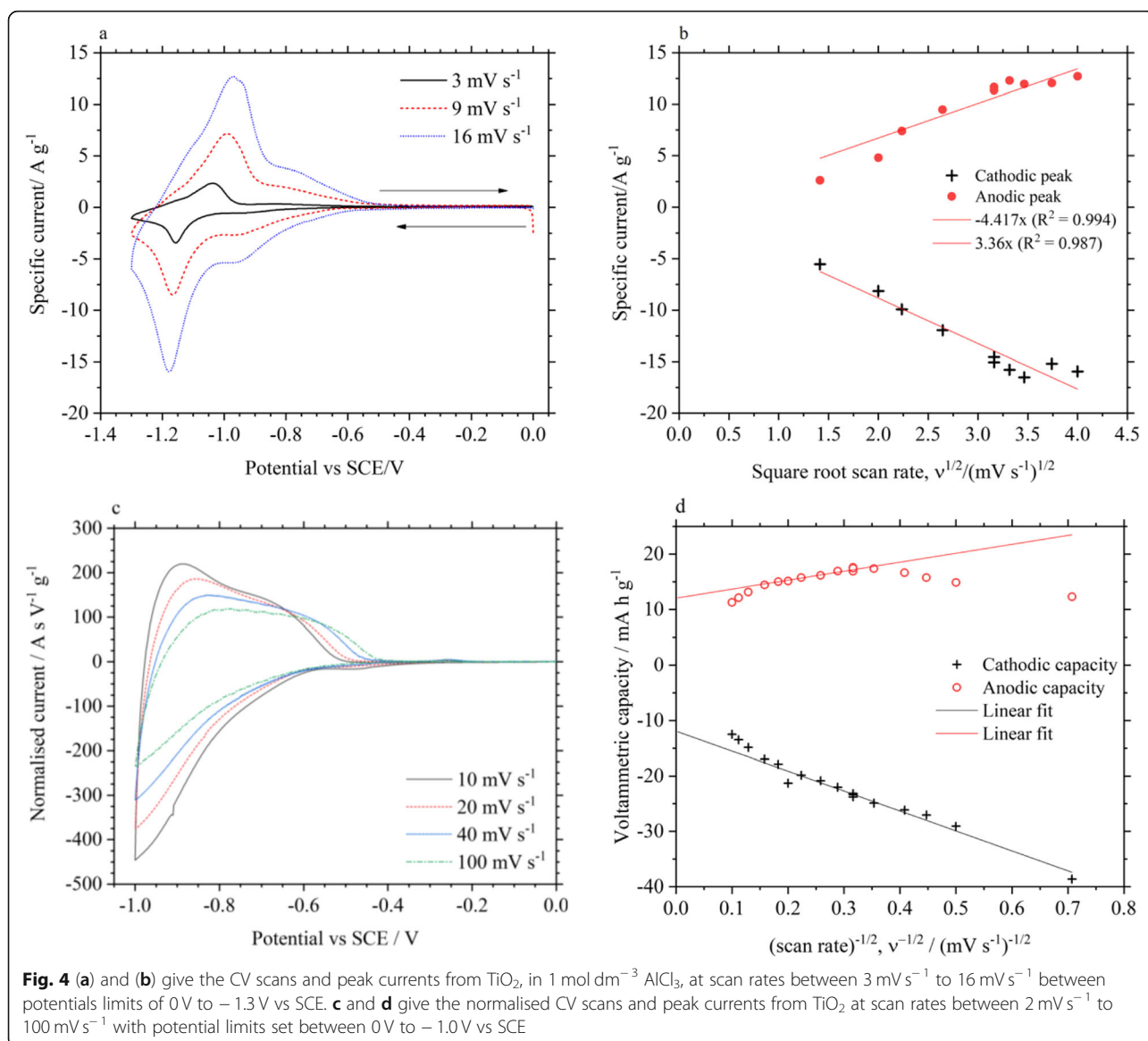
The existence of a surface controlled storage mechanism, along with the mesoporous structure of the 5 nm TiO_2 powder (Fig. 2), suggests performance can be improved through greater electrolyte-electrode contact. In order to achieve this, a simple vacuum impregnation



technique was employed to ensure proper electrode wetting. The experimental set-up and proposed schematic of forced electrode wetting were presented in Fig. 1. It is proposed that electrode pores previously inaccessible to electrolyte, due to surface tension and the hydrophobicity of the nanopowder electrode, are filled with electrolyte due to the removal of air and creation of low pressure voids within the electrode. Constant current cycling was then performed on a vacuum impregnated electrode in a 3-electrode cell between 0.4 V to -1.0 V vs SCE. The coulombic efficiency and discharge capacity of the vacuum impregnated electrode when cycled at specific currents between 0.2 to $40.0 A g^{-1}$ is shown in Fig. 5a. The figure

shows the 10th cycle at a given specific current between cycles 70–120 for as-manufactured TiO_2 and cycles 70–200 for impregnated TiO_2 . For comparison, the performance of an as-manufactured electrode, when cycled up to $6.0 A g^{-1}$, is also shown in Fig. 5a. Additional file 1: Figure S1 shows the discharge capacity and coulombic efficiency of the two electrodes vs cycle number. Between $0.2 A g^{-1}$ and $1.0 A g^{-1}$, discharge capacity from the vacuum impregnated electrode decreases from $21.8 mA h g^{-1}$ to $19.8 mA h g^{-1}$, with coulombic efficiency increasing from 89.8 to 96.9%. At $2.0 A g^{-1}$, coulombic efficiency was 99.4%, though discharge capacity was also measured at $19.8 mA h g^{-1}$. Between $1.0 A g^{-1}$ to $25 A g^{-1}$, discharge capacity

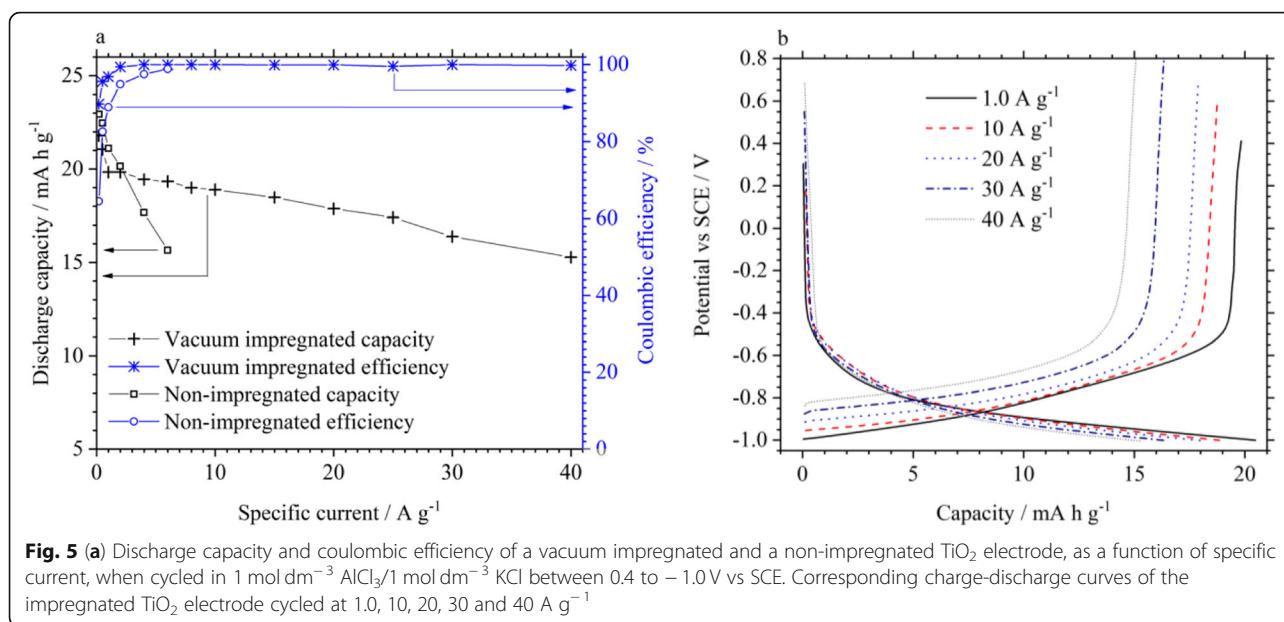




decreased by only 12.2% to 17.4 mA h g^{-1} . At 40.0 A g^{-1} , discharge capacity was measured at 15.3 mA h g^{-1} . Above 2.0 A g^{-1} , coulombic efficiency remained around 99.9%, though some error will be present due to the rapid charge discharge times, i.e. at 40.0 A g^{-1} discharge occurs in 1.43 s, even at the used measurement rate of 80 data points per second. Coulombic efficiency of an as-manufactured electrode is lower throughout and while discharge capacity is comparable up to 2.0 A g^{-1} , once cycled at 6.0 A g^{-1} , discharge capacity was measured at 15.7 mA h g^{-1} compared to $19.33 \text{ mA h g}^{-1}$ for the vacuum impregnated electrode.

The voltage profiles from the vacuum impregnated electrode between 1.0 A g^{-1} to 40 A g^{-1} are given by Fig. 5b. Voltage profiles can be seen to be similar, irrespective of the specific current used. The initial IR-drop at 1 A g^{-1} is minimal, being less than 10 mV and only becoming

noticeable at higher specific currents. At 10.0 A g^{-1} , the IR-drop is measured as 44 mV, increasing to 162 mV at 40.0 A g^{-1} , with the average charge and discharge potentials at 40.0 A g^{-1} being -0.826 V and -0.627 V , respectively. For comparison, the IR drop from the as-manufactured electrode at 6 A g^{-1} was already 124 mV. The results presented in Fig. 5 show a clear improvement in rate capability of electrodes subjected to the vacuum impregnation technique. This specific currents reached are considerably higher than have been previously reported for TiO_2 in aqueous Al^{3+} -containing electrolytes. It should also be noted that the experiment was performed on an electrode with a relatively high mass loading of 6.5 mg cm^{-2} , so that the corresponding current density at 40 A g^{-1} is a very high value of 260 mA cm^{-2} . In comparison, capacities of 50 mA h g^{-1} and ca. 62 mA h g^{-1} were



measured from MnHCF (positive) and graphene (negative) electrodes were achieved at the current density of 5 mA cm⁻² in LiNO₃ [33, 34]. These capacities and current densities are toward the maximum reported for aqueous capacitive devices. Furthermore, the relative stability of the voltage profiles and capacity, where discharge capacity drops by < 25% over an order of magnitude increase in specific current, provides evidence that charge storage from these TiO₂ electrodes in aqueous Al³⁺ electrolyte are predominantly capacitive or controlled by surface reactions at high currents, similar to pseudocapacitive materials. However, care should be taken in describing TiO₂ as pseudocapacitive given the relatively clear voltage plateaus observed during constant current cycling, in aqueous Al³⁺-containing electrolytes, which is in contrast to the electrochemical characteristics of a capacitor.

The vacuum impregnation process was also repeated on a CuHCF electrode, envisaged as a potential positive electrode, with the effect on voltage profiles and capacities at various rates shown in Additional file 1: Figure S2. Capacity from the vacuum impregnated electrode, which had a mass loading of 8.8 mg cm⁻², was measured at 47.08 mA h g⁻¹ at 0.5 A g⁻¹ and maintained a capacity of 28.2 mA h g⁻¹ at 8 A g⁻¹. The capacity of the as-manufactured CuHCF electrode, with a mass loading of 8 mg cm⁻², was 44.42 mA h g⁻¹ at 0.5 A g⁻¹ and decreased to 14.1 mA h g⁻¹ at 6 A g⁻¹. The results demonstrate the applicability of the vacuum impregnation process for improving the performance of alternative electrodes.

Conclusions

Analysis of the CV response from TiO₂ at different scan rates suggested the contribution of a surface controlled

charge storage mechanism. Enhancing this surface contribution was achieved through the application of a vacuum impregnation technique to achieve good electrode wetting and improve electrode-electrolyte contact. This vacuum impregnation step allowed a 1.5 cm × 2 cm, 6.5 mg cm⁻² TiO₂ electrode to maintain a capacity of 15 mA h g⁻¹ at the very high specific current of 40 A g⁻¹ with potential hysteresis between charge and discharge being only 200 mV. A 25% drop in capacity over an order of magnitude increase in specific current adds further evidence to the presence of a surface controlled or capacitive charge storage mechanism from the TiO₂ electrode. The results demonstrate the considerable performance improvements possible from this simple vacuum impregnation technique.

Supplementary information

Supplementary information accompanies this paper at <https://doi.org/10.1186/s42500-019-0010-9>.

Additional file 1. Supplementary materials.

Acknowledgements

The authors would like to acknowledge the financial support received through the European Union's Horizon 2020 research and innovation programme under grant agreement No 646286.

Authors' contributions

AWH (first author, electrochemical analysis), AC (co-supervisor, editing), AZ (BET analysis), AH (experimental design) and RGAW (corresponding author, supervisor, grant holder, electrochemical analysis). All authors have read and approved the final manuscript.

Authors' information

Not applicable.

Funding

This project has received funding from the European Union's Horizon 2020 research and innovation programme under grant agreement No 646286. This contribution was financial only and did not include design of the study or collection, analysis, and interpretation of data or writing the manuscript.

Availability of data and materials

Supporting data and background material can be found in the accompanying supplementary material document.

Competing interests

The authors declare that they have no competing interests.

Received: 8 August 2019 Accepted: 4 December 2019

Published online: 24 December 2019

References

- Kim H, et al. Aqueous rechargeable Li and Na ion batteries. *Chem Rev*. 2014; 114(23):11788–827.
- Kim H, et al. Oxygen vacancies enhance pseudocapacitive charge storage properties of MoO_3-x . *Nat Mater*. 2017;16(4):454.
- Xu J, et al. ACS applied materials & interfaces, 2019; boosting the stable Na storage performance in 1D Oxysulfide. *Adv Energy Mater*. 2019;9(20): 1900170.
- Song W, et al. Pseudo-capacitive Na^+ Insertion in Ti-OC Channels of TiO_2 -C Nanofibers with High-rate and Ultra-stable Performance. *ACS Appl Mater Interfaces*. 2019;11(19):17416–24.
- Zhang BH, et al. Nanowire $\text{Na}_0.35\text{MnO}_2$ from a hydrothermal method as a cathode material for aqueous asymmetric supercapacitors. *J Power Sources*. 2014;253:98–103.
- Hou Z, et al. An aqueous rechargeable sodium ion battery based on a NaMnO_2 - $\text{NaTi}_2(\text{PO}_4)_3$ hybrid system for stationary energy storage. *J Mater Chem A*. 2015;3(4):1400–4.
- Kumar A, et al. An efficient α - MnO_2 nanorods forests electrode for electrochemical capacitors with neutral aqueous electrolytes. *Electrochim Acta*. 2016;220:712–20.
- Long JW, et al. Voltammetric characterization of ruthenium oxide-based aerogels and other RuO_2 solids: the nature of capacitance in nanostructured materials. *Langmuir*. 1999;15(3):780–5.
- Wang W, et al. Hydrous ruthenium oxide nanoparticles anchored to Graphene and carbon nanotube hybrid foam for Supercapacitors. *Sci Rep*. 2014;4:4452.
- Mohajernia S, et al. Semimetallic core-shell TiO_2 nanotubes as a high conductivity scaffold and use in efficient 3D- RuO_2 supercapacitors. *Mater Today Energy*. 2017;6:46–52.
- Tang Z, Tang C-h, Gong H. A high energy density asymmetric Supercapacitor from Nano-architected Ni $(\text{OH})_2$ /carbon nanotube electrodes. *Adv Funct Mater*. 2012;22(6):1272–8.
- Tang Y, et al. Morphology controlled synthesis of monodisperse cobalt hydroxide for supercapacitor with high performance and long cycle life. *J Power Sources*. 2014;256:160–9.
- Meher SK, Rao GR. Ultralayered Co_3O_4 for high-performance Supercapacitor applications. *J Phys Chem C*. 2011;115(31):15646–54.
- Wessells CD, Huggins RA, Cui Y. Copper hexacyanoferrate battery electrodes with long cycle life and high power. *Nat Commun*. 2011;2:550.
- Wessells CD, et al. Nickel Hexacyanoferrate nanoparticle electrodes for aqueous sodium and potassium ion batteries. *Nano Lett*. 2011;11(12):5421–5.
- Shao Y, et al. Design and mechanisms of asymmetric Supercapacitors. *Chem Rev*. 2018;118(18):9233–80.
- Liu S, et al. Aluminum storage behavior of anatase TiO_2 nanotube arrays in aqueous solution for aluminum ion batteries. *Energy Environ Sci*. 2012;5(12): 9743–6.
- Liu Y, et al. The electrochemical behavior of Cl^- assisted Al^{3+} insertion into titanium dioxide nanotube arrays in aqueous solution for aluminum ion batteries. *Electrochim Acta*. 2014;143:340–6.
- He YJ, et al. Black mesoporous anatase TiO_2 nanoleaves: a high capacity and high rate anode for aqueous Al-ion batteries. *J Mater Chem A*. 2014; 2(6):1721–31.
- Kazazi M, Abdollahi P, Mirzaei-Moghadam M. High surface area TiO_2 nanospheres as a high-rate anode material for aqueous aluminium-ion batteries. *Solid State Ionics*. 2017;300:32–7.
- Holland A, et al. An aluminium battery operating with an aqueous electrolyte. *J Appl Electrochem*. 2018;48(3):243–50.
- Liang C, et al. Aqueous batteries based on mixed Monovalence metal ions: a new battery family. *ChemSusChem*. 2014;7(8):2295–302.
- Yao H-R, et al. Rechargeable dual-metal-ion batteries for advanced energy storage. *Phys Chem Chem Phys*. 2016;18(14):9326–33.
- Lu K, et al. A rechargeable Na-Zn hybrid aqueous battery fabricated with nickel hexacyanoferrate and nanostructured zinc. *J Power Sources*. 2016;321: 257–63.
- Holland AW, et al. TiO_2 nanopowder as a high rate, long cycle life electrode in aqueous aluminium electrolyte. *Mater Today Energy*. 2018;10:208–13.
- Yong S, Owen J, Beeby S. Solid-state Supercapacitor fabricated in a single woven textile layer for E-textiles applications. *Adv Eng Mater*. 2018;20(5): 1700860.
- Augustyn V, et al. High-rate electrochemical energy storage through Li^+ intercalation pseudocapacitance. *Nat Mater*. 2013;12:518.
- Lindström H, et al. Li^+ ion insertion in TiO_2 (Anatase). 2. Voltammetry on Nanoporous films. *J Phys Chem B*. 1997;101(39):7717–22.
- Augustyn V, Simon P, Dunn B. Pseudocapacitive oxide materials for high-rate electrochemical energy storage. *Energy Environ Sci*. 2014;7(5):1597–614.
- Yoon S-B, Kim K-B. Effect of poly (3,4-ethylenedioxythiophene) (PEDOT) on the pseudocapacitive properties of manganese oxide (MnO_2) in the PEDOT/ MnO_2 /multiwall carbon nanotube (MWNt) composite. *Electrochim Acta*. 2013;106:135–42.
- Xue Q, et al. LaB_6 nanowires for supercapacitors. *Mater Today Energy*. 2018; 10:28–33.
- Xu J, et al. Capacitive lithium storage of lithiated mesoporous titania. *Mater Today Energy*. 2018;9:240–6.
- Pazhamalai P, et al. Fabrication of high energy Li-ion hybrid capacitor using manganese hexacyanoferrate nanocubes and graphene electrodes. *J Ind Eng Chem*. 2018;64:134–42.
- Lahan H, et al. Anatase TiO_2 as an anode material for rechargeable aqueous aluminum-ion batteries: remarkable Graphene induced aluminum ion storage phenomenon. *J Phys Chem C*. 2017;121(47):26241–9.

Publisher's Note

Springer Nature remains neutral with regard to jurisdictional claims in published maps and institutional affiliations.

Ready to submit your research? Choose BMC and benefit from:

- fast, convenient online submission
- thorough peer review by experienced researchers in your field
- rapid publication on acceptance
- support for research data, including large and complex data types
- gold Open Access which fosters wider collaboration and increased citations
- maximum visibility for your research: over 100M website views per year

At BMC, research is always in progress.

Learn more biomedcentral.com/submissions

